N91-22986

65

MARTIAN IMPACT CRATERS: CONTINUING ANALYSIS OF LOBATE EJECTA SINUOSITY.

N. G. Barlow, SN21, NASA/Johnson Space Center, Houston, TX 77058.

The lobate ejecta morphology surrounding most fresh martian impact craters can be quantitatively analyzed to determine variations in ejecta sinuosity with diameter, latitude, longitude, and terrain. The results of such studies provide another clue to the question of how these morphologies formed: are they the result of vaporization of subsurface volatiles (1) or caused by ejecta entrainment in atmospheric gases (2). Kargel (3) provided a simple expression to determine the degree of non-circularity of an ejecta blanket. This measure of sinuosity, called "lobateness", is given by the ratio of the ejecta perimeter to the perimeter of a circle with the same area as that of the ejecta:

$$\Gamma = \text{perimeter}/(4\pi*\text{area of ejecta})^{1/2}.$$

A circular ejecta has a Γ of 1; more sinuous ejecta display $\Gamma>1$. Kargel's study of 538 rampart craters in selected areas of Mars led him to suggest that lobateness increased with increasing diameter, decreased at higher latitudes, and showed no dependence on elevation or geologic unit.

Major problems with Kargel's analysis are the limited size and distribution of his data set and the lack of discrimination among the different types of lobate ejecta morphologies (4). Bridges and Barlow (5) undertook a new lobateness study of 1582 single lobe (*SL*) and 251 double lobe (*DL*) craters. Their results are summarized in Tables I and II. These results agree with the finding of Kargel that lobateness increases with increasing diameter, but found no indication of a latitude dependence for *SL* craters. A slight terrain dependence was also detected, contrary to Kargel's results.

The Bridges and Barlow study has now been extended to multiple lobe (*ML*) craters. Three hundred eighty *ML* craters located across the entire martian surface have been studied. *ML* craters provide more complications to lobateness studies than do *SL* or *DL* craters--in particular, the ejecta lobes surrounding the crater are often incomplete (i.e., do not extend completely around the crater). Since the lobateness formula compares the perimeter of the ejecta lobe to that of a circle, we have restricted our analysis only to complete lobes. The lobes are defined sequentially starting with the outermost lobe and moving inward: L1 for the outermost lobe, L2, L3, etc. for inner lobes. Generally only two or three complete lobes are recognizable for *ML* craters.

Median lobateness values for the lobes are 1.18 for L1, 1.13 for L2, and 1.09 for L3. The L1 value is slightly larger than the average *SL* and *DL* lobateness values. L2 lobateness values are comparable to those found for the highland *SL* craters and for the outer lobe (L1) of *DL* craters. L3 lobateness values are equal to Γ values of plains *SL* craters and the inner lobe (L2) of *DL* craters. Analysis of individual craters show that 72% of the L2 lobes display smaller Γ than their accompanying L1, and, in 77% of craters with three lobes, L3 has a lower Γ than L2. Eighty-nine percent of all craters with three lobes show L3 with less sinuous ejecta (i.e., lower Γ) than L1. This continues the trend seen with *DL* craters. No statistically significant lobateness dependence on latitude is suggested for L1, L2, or L3. Kargel's detection of a latitude-lobateness correlation can be explained by Barlow and Bradley's (6) observation of more *ML* craters (which have higher Γ) near the equator and more *SL* craters (with lower Γ) near the poles. Since Kargel did not distinguish among different ejecta morphologies, he inadvertently reported

a lobateness relationship with latitude. Also contrary to Kargel's study, we found that *ML* craters on highlands regions tend to show slightly lower values of lobateness than *ML* craters on plains, at least for the L1 (Γ_h=1.17; Γ_p=1.20) and L2 (Γ_h=1.13; Γ_p=1.15) lobes. This is opposite the trend seen for *SL* craters, where lower lobateness values are seen for craters on the plains.

The change in Γ with increasing diameter suggests that either impact energy or changes in physical properties with depth are reflected in ejecta sinuosity measurements. However the change in Γ with general geologic unit and ejecta morphology (which varies with latitude (see 6)) favors a dependence of sinuosity on target properties. This in turn has implications for the distribution of volatiles on Mars, if we accept the theory that fluidized ejecta morphologies result from impact vaporization of subsurface volatiles (1). If increases in Γ correspond to higher volatile-to-clast ratios, the correlation of Γ with diameter, morphology, and geologic unit implies that the highlands are volatile-rich close to the surface and plains have volatile reservoirs stored at greater depths. Alternately, if *SL* craters form by impact into ice and *ML* craters result from excavation into subsurface aquifers (as suggested by (6, 7)), these same correlations lead us to conclude that the highlands are icier than the plains but the plains contain more near-surface water.

References: (1) Carr, M.H. et al. (1977), *JGR*, **82**, 4055. (2) Schultz, P.H. and Gault, D.E. (1979), *JGR*, **84**, 7669. (3) Kargel, J.S. (1986), *LPS XVII* (abs.), 410. (4) Mouginis-Mark, P. (1981), *JGR*, **84**, 8011. (5) Bridges, N.T. and Barlow, N.G. (1989), *LPS XX* (abs.), 105. (6) Barlow, N.G. and Bradley, T.L. (1990), submitted to *Icarus*. (7) Johansen, L.A. (1979), NASA TM 80339, *Rpts. Planet. Geol. Geophys. Prog. 1978-1979*, 123.

Table I--General Results of Lobateness Studies

	SL		DL		ML		
	P	H	L1	L2	L1	L2	L3
Number	370	1212	251	245	380	363	184
Median Γ	1.09	1.13	1.14	1.09	1.18	1.13	1.09
Max Γ	3.33	3.81	2.27	1.38	1.74	1.47	1.33
Min Γ	1.00	1.01	1.01	1.00	1.02	1.01	1.00
Average Γ	1.13	1.16	1.17	1.10	1.20	1.16	1.10
Latitude Dep?	No	No	*	*	No	No	No

P - Northern Plains   H - Southern Highlands

*DL craters are located primarily within the 40-65°N latitude range, thus latitude dependence studies are not valid.

Table II--Median Γ Values by Diameter Range

Diam (km)	SL		DL		ML		
	P	H	L1	L2	L1	L2	L3
8.0-11.3	1.09	1.11	1.13	1.07	1.11	1.06	1.06
11.3-16.0	1.09	1.14	1.14	1.07	1.12	1.09	1.07
16.0-22.6	1.12	1.16	1.17	1.10	1.17	1.13	1.08
22.6-32.0	1.15	1.18	1.17	1.13	1.20	1.18	1.11
32.0-45.3	1.08	1.17	1.30	1.24	1.22	1.18	1.12
45.3-64.0	--	1.11	1.08	1.17	1.27	1.33	1.22
64.0-90.5	--	--	--	--	1.35	1.27	1.18

CAN IRON OXIDE/OXYHYDROXIDE MINERALS BE IDENTIFIED ON THE MARTIAN SURFACE FROM GROUNDBASED VIS-NIR SPECTRA?

Jim Bell and Tom McCord, Planetary Geosciences, Univ. Hawaii, Honolulu 96822; BITNET: jimbo@uhpgvax.pgd.hawaii.edu

Visible to Near-Infrared (VIS-NIR) reflectance data of numerous regions on Mars were obtained during the 1988 opposition at Mauna Kea Observatory. A Circular Variable Filter (CVF) spectrometer was used to acquire data of 41 regions on the planet from 0.4-1.0 μm. The spatial resolution of these observations was approximately 500-600 km, the spectral resolution was R = $\lambda/\Delta\lambda$ $\simeq$ 80, and the spectral sampling was S $\simeq$ 125 channels/μm [Bell et al., 1989].

The new CVF data show abundant evidence (some previously observed, some not) of the existence of the Fe^{3+} cation on Mars. First, there is the strong and diagnostic $O^{2-} \rightarrow Fe^{3+}$ near-UV charge transfer absorption edge which is typical of ferric-bearing minerals [e.g., Sherman et al., 1982]. This deep blue absorption is primarily responsible for the red color of Mars and also lead numerous early workers to speculate on the existence of iron oxides on the martian surface. Second, there is a weaker though clearly discernible absorption band from 0.78-0.94 μm, centered at $\simeq$ 0.85 μm in many of the spectra. This band has been interpreted by several groups as being due to the $^6A_1 \rightarrow {}^4T_1(^4G)$ ligand field transition of Fe^{3+} [Singer, 1982; Morris et al., 1989; Bell et al., 1989], indicating the presence of some crystalline iron oxide component in the Mars soil. This contention is further supported by the third piece of evidence, a heretofore undetected weak band or "cusp" at 0.61-0.72 μm that is interpreted as being due to the $^6A_1 \rightarrow {}^4T_2(^4G)$ electronic transition of Fe^{3+}. This weak feature is typically deepest in spectra of brighter regions on the planet. Thus these new data indicate unambiguous evidence of Fe^{3+} absorption; the question as posed above is whether or not the positions and strengths of these absorptions can be used to identify surface Fe^{3+} mineralogy.

Some of these new data are compared directly to laboratory Fe^{3+}-bearing mineral spectra in Figures 1-3. It can be immediately seen that the position and strength of the near-UV charge transfer absorption edge places severe constraints on the abundances of several of these pure iron oxides in certain particle size ranges. For example, the hematite powder in Figure 1 exhibits a steep, saturated near-UV absorption with the band edge near 0.55 μm, typical of most bulk crystalline hematites and a poor match to the martian spectral data. It can be seen that none of the other common iron oxides/oxyhydroxides in Figure 1 reproduce the shape and position of the near-UV absorption either. The less common and also more poorly crystallized Fe^{3+} phases in Figure 2 come closer to matching the absorption edge position and shape, yet there are still discrepancies except for the spectrum of synthetic iron-silica gel which provides a fair match. The similarly poorly crystalline "amorphous" palagonites in Figure 3 also provide a good fit to the absorption edge. Based on this simple examination of these particular lab data, it appears that poorly crystalline (not amorphous) materials exhibit the best match to the VIS-NIR martian data based solely on the highly diagnostic near-UV charge transfer absorption.

As mentioned above, however, two crystalline Fe^{3+} absorption bands are evident in the new Mars data. Figure 3 clearly shows that most "amorphous Hawaiian soils" such as those examined by Singer (1982) do not exhibit Fe^{3+} bands as deep as those in the Mars data, suggesting then that although poorly crystalline materials constitute an important part of the Mars soils, some component of well crystallized, bulk Fe^{3+}-bearing mineral(s) exist and produce those features. A more quantitative estimate of the partitioning of crystalline vs. poorly crystalline Fe^{3+} phases is in progress.

A quick look at the variation in band strengths and positions of the two VIS-NIR Fe^{3+} electronic transition bands in the lab data of Figures 1 and 2 suggests that the answer to the question posed in the title is "yes." The increased spectral sampling of these new data combined with ongoing lab analog studies and refined data calibration suggest that at least hematite, and possibly also goethite, existing in a wide range of particle sizes down to nanometer scales, may be important constituents of the Mars soil. Other possibilities which must not be overlooked without further study include Fe^{3+}-bearing sulfates, palagonite-like secondary weathering products, and some of the more exotic, poorly crystalline iron oxides/oxyhydroxides.
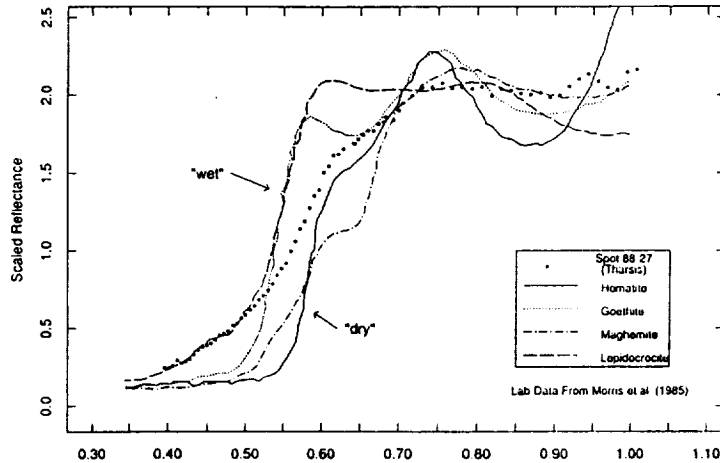
Figure 1: Mars CVF spectrum 88-27 (Tharsis region) from Bell *et al.* (1989) compared to four common iron oxides/oxyhydroxides. The lab data are from powdered samples of Morris *et al.*, 1985. The wet/dry distinction simply refers to the presence or lack of OH$^-$ radicals in the mineral structure. Note the poor fit of the Mars data to the lab near-UV charge transfer absorptions and the variation of position of the two Fe^{3+} electronic transitions at 0.65 μm and 0.86 μm in the lab data. Data scaled for display purposes.
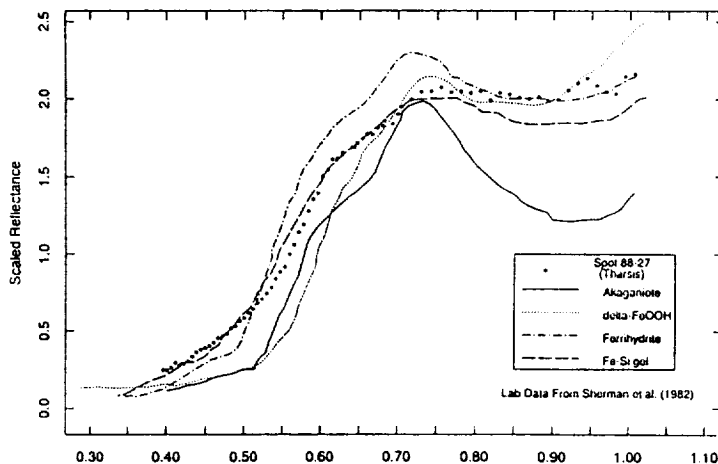
Figure 2: Same Mars data as Figure 1 compared to some less common and poorly crystalline iron oxides/oxyhydroxides from Sherman *et al.*, 1982. The near-UV charge transfer edge is more closely matched in these data although there are still discrepancies. Data digitized and scaled for display purposes.
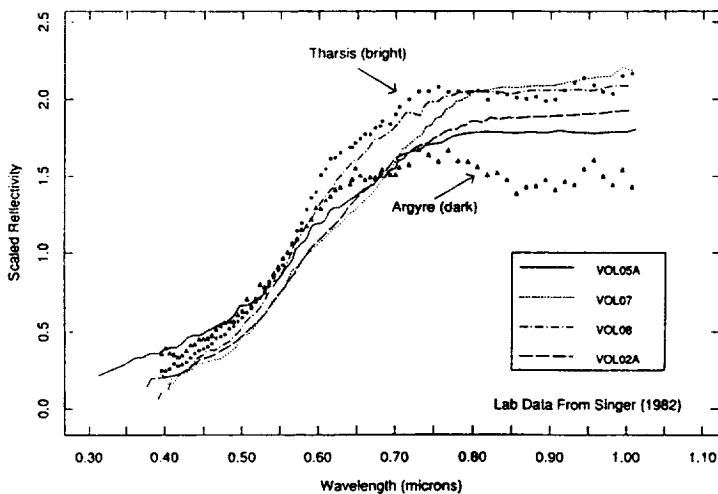
Figure 3: Mars CVF data from bright (Tharsis) and dark (Argyre) albedo regions compared to hawaiian palagonite spectra of Singer (1982). The position of the near-UV charge transfer edge is matched nicely, however the palagonites show little evidence of the crystalline Fe^{3+} absorption bands seen in the Mars data. Data digitized and scaled for display.

References:

Bell, Jim, T.B. McCord, and P.D. Owensby (1989) submitted to *JGR, Special Mars Conference Issue*.

Morris, R.V., H.V. Lauer, Jr., C.A. Lawson, E.K. Gibson, Jr., G.A. Nace, and C. Stewart (1985) *JGR*, *90*, 3126-3144.

Morris, R.V., D.G. Agresti, H.V. Lauer, Jr., J.A. Newcomb, T.D. Shelfer, and A.V. Murali (1989) *JGR*, *94*, 2760-2778.

Sherman, D.M., R.G. Burns, and V.M. Burns (1982) *JGR*, *87*, 10169-10180.

Singer, R.B. (1982) *JGR*, *87*, 10159-10168.

GROUNDBASED IMAGING SPECTROSCOPY OF MARS DURING 1988 AND 1990: INSTRUMENTATION AND DATA REDUCTION/INTERPRETATION STRATEGIES FOR THE FUTURE OF PLANETARY SPECTROSCOPY: Jim Bell, Paul Lucey, Tom McCord, and Tom Ozoroski, HIG/PGD, Univ. Hawaii, Honolulu 96822; BITNET: jimbo@uhpgvax.pgd.hawaii.edu

Our goals for the 1988 and upcoming 1990 Mars oppositions are to map the surface of Mars at 150-250 km resolution in the 0.4-2.5 μm range using imaging spectroscopy. One of the great advantages of imaging spectroscopy over traditional narrow-band filter imaging or point spectroscopy is its ability to obtain simultaneous information over wide spatial and spectral ranges [1,2]. Such measurements produce enormous quantities of data, on the order of 10-100 Mbytes per night of observing. Obviously, this is a concern that must be addressed by the proper choice of image processing hardware and software. Depending on the size of the array used, 10^4 - 10^6 *individual* spectra can be produced from any single dataset. This huge number prohibits traditional methods of spectrum interpretation, and thus techniques must be derived which can automatically analyze vast numbers of spectra and produce maps of the most important quantities.

For example, we obtained imaging spectrometer data of 70% of the martian surface in the 0.4-1.0 μm range from Mauna Kea Observatory during the 1988 opposition [2,3]. Using the U.H. 2.24-m Wide Field Grism Spectrograph and IFA/Galileo CCD, 26 raw Mars and standard star image cubes of dimensions 800 X 200 X 50 (spatial X spectral X spatial) were obtained. Standard spectral and CCD data processing techniques required some 75 hours of continuous processing by a 2 MIPS Sun 3/260 machine just to obtain approximately calibrated reflectance images. After performing this level of reduction we employed several techniques to simplify our analyses. One technique was band-depth mapping. Our 0.4-1.0 μm image cube spectra showed Fe^{3+} absorption bands at 0.65 μm and 0.86 μm which varied spatially on the planet. In a manner similar to lunar spectrum continuum removal, we created an averaged image across the 0.61-0.72 μm region and ratioed that with an image at 0.68 μm. The resulting ratio image shows several classical bright regions on Mars to exhibit up to a 5% deeper 0.65 μm Fe^{3+} band than dark albedo regions, consistent with the idea of bright regions consisting of more weathered (dusty) materials. Possibly of more interest, however, are several regions on the planet where the Fe^{3+} band variations do not correlate well with observed classical albedo boundaries, such as Sinus Sabaeus (Figure 7 in [2]).

A second technique used in data analysis was polynomial fit coefficient mapping [4,5]. In this process, the spectral axis is fit to an nth order polynomial $(y=a_nx^n+a_{n-1}x^{n-1}+...+a_0)$, yielding n+2 (including residuals) coefficients for each pixel that can subsequently be displayed as n+2 complete images showing how these coefficients vary across the martian surface. Some examples of this procedure are shown in Figs. 1 and 2. In Fig. 1 the steep near-UV Fe^{3+} absorption edge characteristic of Mars [e.g. 6, 7] was fit by a first order polynomial, and the resulting spectral slope and intercept are plotted as images. The intercept maps correlate very well with albedo (as expected: albedo is just an additive offset), and the spectral slope also shows significant correlation, again consistent with classical bright regions having "redder" spectra. However, several regions near the south polar cap (300-360° W) and west of Sinus Meridiani in Thaumasia (near 30°S, 60-90° W) are anomalous in that they do not show the typical global slope/albedo correlation. In Fig. 2 similar maps are presented for a fit to near-infrared data from 0.735-0.795 μm. Again the spectral intercept is essentially an albedo map, but the slope maps are relatively "bland" and somewhat noisy, consistent with the fact that the martian spectrum is relatively flat to slightly "blue" at these wavelengths [6,7]. For the slope maps, brighter values indicate deeper "near-infrared" absorption. There is some structure in these images associated with the Sinus Meridiani/Sinus Sabaeus region, showing the northern boundary of this dark albedo feature to have a relatively flat spectrum while its southern boundary has a deep (most likely Fe^{3+}) absorption. Such anomalous regions may indicate more spectral heterogeneity than once thought in the martian surface fines, and are difficult to detect using standard imaging or point spectroscopy techniques.

Observing plans for the upcoming 1990 opposition (the last in the excellent 1986-1988-1990 triad) include further mapping of the entire planet in the 0.4-1.0 μm and 1.0-2.5 μm regions. For the longer wavelength imaging spectrometer data we will concentrate our efforts on the Tharsis/Valles Marineris region in an effort to directly compare our global dataset with the higher resolution though spatially confined Phobos-2 ISM data [8]. Also, an in-depth analysis of the Syrtis Major/Sinus Sabaeus area will be undertaken in an effort to characterize better the compositional nature of the dark regions (can we really see exposed "bedrock?" [9]) and provide comparisons to high spatial resolution 1988 groundbased images of the same areas [10].
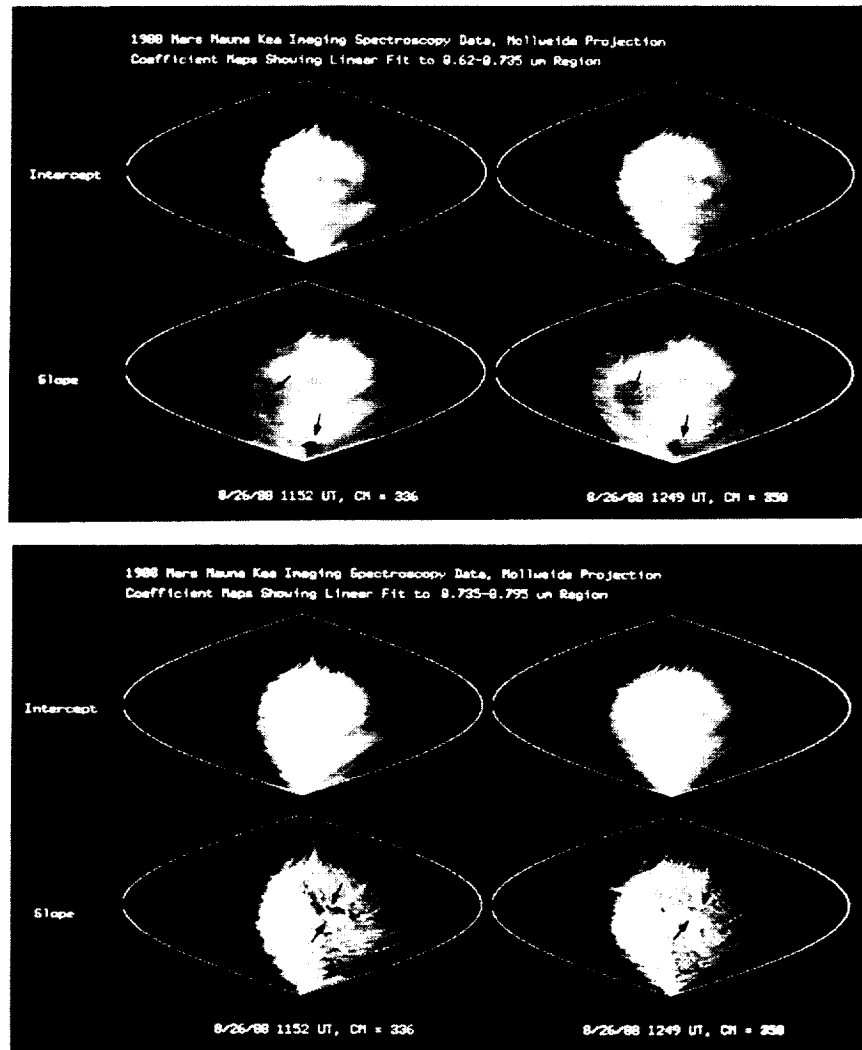

Figure 1 (Top) and Figure 2 (Bottom). See text for explanation.

References: [1] Goetz A.F.H., Vane G., Solomon J.E. and Rock B.N. (1985) *Science, 228,* 1147-1153. [2] Bell III J.F., McCord T.B., and Lucey P.G. (1990) *Proc. Lunar Planet. Sci. Conf. 20th,* 479-486. [3] Bell III J.F., McCord T.B., and Lucey P.G. (1989) *EOS Trans. AGU, 70,* 50. [4] Lucey P.G., Bruno B.C., and Hawke B.R. (1989) *B.A.A.S., 21,* 971. [5] *Ibid* . (1990) *LPSC XXI,* 726-727. [6] McCord T.B. and Westphal, J.A. (1971) *Astrophys. J., 168,* 141-153. [7] Bell III, J.F., McCord, T.B., and Owensby, P.D. (1990) *J. Geophys. Res.,* in press. [8] Bibring, J.-P. and 16 others (1989) *Nature, 341,* 591-593. [9] Zimbelman, J.R. and Craddock, R.A. (1990) *LPSC XXI,* 1377-1378. [10] Pinet P. and Chevrel S. (1989) submitted to *J. Geophys. Res.*

COMPARISON OF NEW GROUNDBASED AND PHOBOS-2 VSK COLOR RATIO DATA FOR MARS;

James F. Bell III[1,2], Mark S. Robinson[1], Thomas B. McCord[1,3], and Fraser P. Fanale[1] ([1]Planetary Geosciences Division, Univ. of Hawaii, Honolulu 96822; [2]Remote Sensing Lab, Univ. of Washington AJ-20, Seattle 98195; [3]SETS, Inc., Mililani, HI 96789)

Summary: The VSK-FREGAT imaging experiment on the Phobos-2 spacecraft acquired several VIS (0.4-0.61 μm) and NIR (0.7-1.1 μm) image pairs containing both Mars and Phobos during February and March, 1989 [17]. We have analyzed these image pairs and calculated NIR/VIS DN ratios for Mars for comparison with groundbased 0.4-1.0 μm CVF reflectance spectra obtained during August, 1988 [1]. We find that for the particular region imaged (Mare Sirenum, 35°S, 155°W--NE of Newton crater) our telescopic reflectance spectrum convolved to VSK bandpasses yields a NIR/VIS ratio of 1.78. The NIR/VIS DN ratio that we obtained from Phobos 2 image pairs at similar phase angles as the groundbased data is 2.25±0.2, thus suggesting that dividing such Mars (and Phobos) DN ratios by a correction factor of 1.26 yields more accurate values for the true NIR/VIS reflectance ratio. Several sources of error, including near-opposition contrast enhancement in the blue ("blue clearing") associated with possibly variable atmospheric dust loading between August 1988 and February-March, 1989 indicate that this method of calibration could possibly suffer from additional errors of up to 10-15%, although comparison of the Phobos-2 data with Viking results [5] seems to indicate that these effects were minimal or absent during the 1989 encounter.

Discussion: Current efforts to map color variations (and thus perhaps map compositional variations [2,5]) are using calibration methods based on modeled groundbased telescopic narrow-band filter photometer data of Mars (R ≈ 20; [e.g. 3,4]) compared against the spacecraft VIS and NIR image pairs that contain both Mars and Phobos [5]. After having discovered that one of the regions we measured in August 1988 was also serendipitously imaged by Phobos-2 (S. Murchie, personal communication, 1989), we decided to use these new, higher spectral resolution data to better constrain the ongoing color calibration efforts [5,6].

Using the data from [7] we plotted a smoothed solar spectrum for the 0.4-1.1 μm region and multiplied this spectrum by our reflectance data for CVF Spot 88-37 (Figure 1). Thus we obtained a spectrum that we then convolved into the VSK VIS and NIR bandpasses that simulates the response that the Phobos-2 cameras recorded of the same region on Mars some six months later. Ignoring absolute flux levels since we are most interested in obtaining the VIS/NIR channel *ratio* and using a NIR/VIS filter efficiency ratio of 1.395 (B. Zhukov, personal communication, 1989) we determined that if the VSK experiment had been looking at a region on Mars which exhibits a reflectance identical to that of our CVF Spot 88-37, then it would have obtained a NIR/VIS DN ratio of 1.78 (for comparison, [5] obtained NIR/VIS = 2.08). Additionally, we found that given the above parameters and a NIR/VIS bandpass solar flux ratio of 0.806, the NIR/VIS DN ratio of a constant albedo object as viewed by VSK would be 1.125.

Using dark subtracted, flatfielded, and recently re-calibrated [5] VSK images of Phobos and Mars, we determined average DN values and variations for the region of Mars common to our spectral data in images 2300123 and 2300111. Data values for 17X17 pixel regions for the NIR and VIS channels were 62±3.5 and 110±3, respectively. The VIS image had an exposure 4 times that of the NIR, so assuming that the cameras were linear the resulting NIR/VIS image ratio was 2.25±0.19.

A possible source of error in the comparison with groundbased results is the so-called "blue clearing" or near-UV brightening near zero phase. This effect (which is difficult to quantify) is typically strongest during periods near perihelion in southern hemisphere spring and summer (Ls≈160-200° and Ls≈270-300° [8]). Visual monitoring during our telescopic observations, acquired at Ls=250° and a phase angle of 34° did not show any indications of this phenomenon, however imaging spectrometer data that we obtained six weeks later at opposition (near zero phase) did show distinct evidence of increased contrast in the blue [9,10], suggesting that significant changes in reflectivity can occur in global or localized areas on Mars over short timescales. Comparisons of these telescopic spectra (and others such as those of

[3,4]) with the Phobos-2 imaging data, acquired at $L_s=3°\text{-}17°$, may exhibit systematic variations of up to 5-10% due to such variations in flux in the visible.

A related source of variability is atmospheric dust load changes between August 1988 and February-March 1989. Variations in column abundance and/or surficial distribution of bright, very red dust particles (which may be the cause of brightening in the blue) are known to occur on both diurnal and seasonal timescales, with the greatest variability typically occurring near and shortly after perihelion when insolation is a maximum [11,12]. Fe^{3+}-rich dust will produce systematic variations mostly in the Phobos-2 NIR imaging channel due to its higher reflectance from 0.7-1.1 μm than from 0.4-0.61 μm [1,13]. Although difficult to quantify and highly longitudinally dependent, we estimate that variations in dust opacity over a low albedo region such as Sirenum can easily lead to 10-15% reflectance variations at NIR wavelengths for localized dust storms, or possibly up to 50% reflectivity variations during truly global dust storms that completely obscure the surface below [see also 14,15].

The combined effect of these VIS and NIR variabilities on the final NIR/VIS DN ratios is to introduce possibly significant uncertainty (perhaps as much as 10-15%) in the comparison with groundbased reflectance data which have not been simultaneously obtained. Unfortunately, we know of no 0.4-1.1 μm reflectance spectra of Mars obtained during February-March 1989 other than the Phobos-2 ISM imaging spectrometer data [16], which only extend down to 0.8 μm and did not image the Sirenum region. Preliminary work comparing Viking Orbiter and Phobos-2 color ratios of Phobos [5] seem to indicate, however, that these effects may not be serious for these data, thus allowing increased confidence in color unit mapping efforts.

References: [1] Bell III, James F., T.B. McCord, and P.D. Owensby (1989), submitted to JGR Special Fourth Mars Colloquium Issue. [2] Murchie, S., D.T. Britt, J.W. Head, S.F. Pratt, B.S. Zhukov, and A.A. Kuzmin (1989), B.A.A.S., 21, 957. [3] McCord, T.B. and J.A. Westphal (1971), Astrophys. J., 168, 141-153. [4] McCord, T.B., R.L. Huguenin, D. Mink, and C. Pieters (1977), Icarus, 31, 25-39. [5] Murchie, S. and 12 others (1990), LPSC XXI, this volume. [6] Bell, Jeffrey F., P.G. Lucey, J.C. Gradie, J.C. Granahan, D.J. Tholen, J.R. Piscitelli, and L.A. Lebofsky (1989), B.A.A.S., 21, 991. [7] Allen, C.W. (1973), Astrophysical Quantities, pp. 171-173. [8] Slipher, E.C. (1962), Mars: The Photographic Story, pp. 37-54. [9] Bell III, James F., T.B. McCord, and P.G. Lucey (1989), Proc. 20th Lunar Planet. Sci. Conf., in press. [10] Bell III, James F., T.B. McCord, P.G. Lucey (1989), EOS, Trans. Amer. Geophys. U., 70, 50. [11] Martin, L.J. (1974), Icarus, 23, 108-115. [12] Zurek, R.W. and L.J. Martin (1989), B.A.A.S., 21, 980. [13] Singer, R.B. (1982), JGR, 87, 10159-10168. [14] Pollack, J.B., D.S. Colburn, F.M. Flaser, R. Kahn, C.E. Carlston, and D. Pidek (1979), JGR, 84, 2929-2946. [15] Briggs, G.A., W.A. Baum, and J. Barnes (1979), JGR, 84, 2795-2820. [16] Bibring, J.-P. and 16 others (1989), Nature, 341, 591-593. [17] Avanesov, G.A. and 43 others (1989), Nature, 341, 585-587.
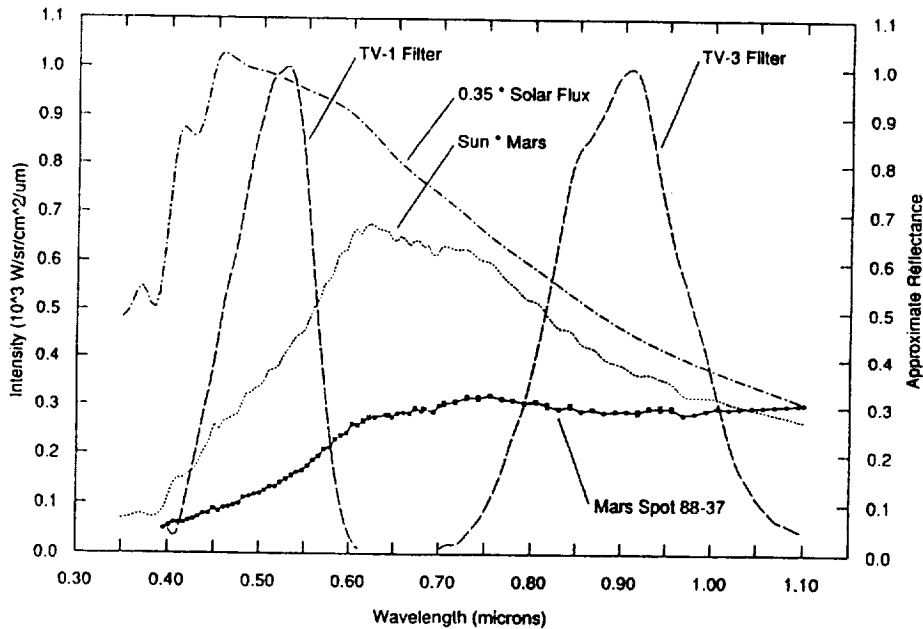

Figure 1: 1988 Mars CVF reflectance data (scale at right), Phobos-2 VSK bandpasses (normalized to 1.0) [17] and Solar Flux [7] and Mars*Solar Flux data (scale at left).

Iron-enriched Smectite Clays as Mars Soil Analogs - Chemical Reactivity in the Labeled Release Experiment; T. Ben-Shlomo and A. Banin, Department of Soil and Water Science, The Hebrew University, Rehovot, Israel.

On the basis of the martian soil elemental composition directly determined by the Viking landers, and through a computerized modelling-search it was proposed that the soil may contain phyllosilicate minerals of the smectite group mixed with iron oxides, and small amounts of carbonates and sulfate salts (1). Following this model and other data, it was suggested that significant amounts of iron in the martian soil may be associated with the smectite clays as adsorbed-precipitated oxide or oxyhydroxy iron phases (2, 3). In order to further examine this model a series of iron-enriched clays, containing iron at concentrations up to that found in Mars soil (ca. 19% Fe_2O_3) was prepared from a standard montmorillonite (SWy-1, the Clay Minerals Society) by the "Quantitative Ion Exchange Method" (4). The chemical and mineralogical properties of the clay and of the iron phase(s) formed in the system have been determined. The clay preparation procedure caused little change in the crystal lattice thus producing purified montmorillonite clay free of soluble salts and minor accessory minerals but with the predesignated proportion of adsorbed iron and precipitated iron oxides and oxyhydroxides, characterized by the chemical analysis and morphological study to be poorly ordered and of low crystallinity (5).

Reflectance spectra in the visible and near-IR wavelength range revealed increasing absorbance below $0.7 \mu m$ with the increased iron addition. Such absorbance is characteristic to the Mars spectra. A broad absorbance band around $0.9 \mu m$ was also developed as more iron was added . It was also found during recent telescopical observations (6). However, the pronounced spectral features of crystalline smectite in the near-IR (2.1-$2.3 \mu m$) and in the IR range (doublet at $20 \mu m$) were not detected in the martian spectra (7, 8), indicating that crystalline smectite may not be a singular silicate phase in the martain soil.

Simulation of the Viking Landers Labeled Release (LR) experiment were carried by the ^{14}C absorption method ("Getter Technique") (2) with: (a) Iron enriched clays, prepared by chemical deposition by the quantitative ion exchange method, in which the concentration of added iron ranged from below the exchange capacity of the clay up to $\sim 15\% Fe_2O_3$ bringing the total iron content to that found in the martain soil (Fig. 1). (b) A physical mixture of various crystalline iron oxides (maghemite, goethite and hematite) and short-range-ordered ferrihydrite with iron-saturated clay (Fe-Mont, $7\% Fe_2O_3$) at a constant added concentration of 12%wt Fe_2O_3, which add-up to the iron concentration found in the martain soil (Fig. 2). (c) Same as (b) but mixed with the crude SWy-1 montmorillonite (which was found to be nonactive during the LR simulation, probably for increasing the pH values) (Fig 2). (d) Same as (b) but the clay was mixed with 24%wt siderite ($FeCO_3$) (Fig. 2).

The presence of excess non-crystalline or poorly crystalline iron oxides at a high concentration beyond the exchange capacity systematically decreased the reactivity of the mixture (Fig. 1). However, iron-adsorbed clay ($\sim 7\% Fe_2O_3$) alone or when mixed with crystalline iron oxides up to $19\% Fe_2O_3$ in series (b), and with siderite (d), exhibited good match to the decomposition rate found on Mars (Fig. 2). The crystalline iron oxides mixed with the crude SWy-1 montmorillonite in series (c) did not simulate the LR reaction (Fig. 2). Levin and Straat reported also that hematite alone was not active in simulation of the LR reaction (9). The effect of the mixing of the less crystallized ferrihydrite with the iron clay in diminishing the reactivity (Fig. 2), is notably similar to that of the amorphous iron-oxides formed in situ (series a, Fig. 1). Addition of siderite to the iron clay did not cause a pronounced change in the decomposition rate (Fig. 2) although the addition of 12%wt magnesite ($MgCO_3$) or dolomite ($CaMg(CO_3)_2$) and only 2% calcite ($CaCO_3$) substantially decreased the decomposition reaction (data not shown).

(Iron Smectite - Mars Soil Analogs) Ben-Shlomo T. and Banin A.

It was suggested that the formate decomposition mechanism by the iron clay is mainly dehydrogenation, involving electron transfer to adsorbed Fe^{3+} (2). The presence of excess amorphous iron oxide or oxyhydroxide precipitates, may perhaps interfere with this reaction partly by adsorbing the formate to the iron oxyhydroxide.

Thus, the presence of iron oxides per se is not sufficient to drive the decomposition reaction, and the iron phase(s) crystallinity and surface properties affect the kinetics and extent of the reaction. The presence of the reactive surface of iron smectites seems to be essential for the decomposition reaction measured by the Viking landers in the LR experiment.

References:
(1) Toulmin, P. III, Baird A.K., Clark B. C., Keil K., Rose H. J., J.R., Christian, R.P., Evans P.H. and W.C. Kelliher (1977) JGR 82, 4625-4634 (2) Banin, A. and Rishpon J. (1979) J. Mol. Evol. 14, 133-152. (3) Banin, A. (1986) "Clays on Mars", In Clays and the Origin of Life (H. Hartman and A.G. Cairns-Smith, eds.) pp. 106-115. (4) Banin A. (1973) U.S. Patent 3,725,528 April 3,1973 14pp. (5) Ben-Shlomo, T. and Banin A. (1989) submitted to the Proceedings of the 9th International Clay Conference. (5) Singer, R. B. (1982) JGR 87:10,159-10,168 (6) Bell, J. F., McCord T.B. and Owensby P.D. (1989) submitted to JGR special 4th Mars colloquium issue.(7) Roush, T. B., Pollack B. J. and Banin A. (1989) in the Fourth International Conference on Mars, Tucson, Arizona, January, 1989. (8) Ben-Shlomo, T. and Banin A. (1989) in the International Symposium on First Results of the Phobos-Mars Mission and Future Space Exploration, Paris, Oct. 1989. (9) Levin, G. V. and Straat P. A. (1981) Icarus 45:494-516. (This work was supported in part by the NASA Exobiology and Solar System Exploration Programs).
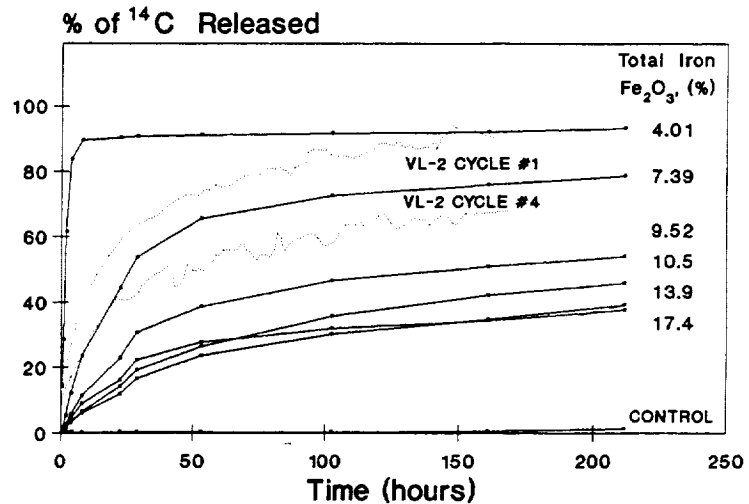
Fig. 1: Decomposition of the LR medium by Mars soil in the Viking Labeled Release Experiment (VL-2), and in simulation experiments with sodium formate using H-Mont. (4.01%Fe$_2$O$_3$), Fe-Mont. (7.39%Fe$_2$O$_3$) and various iron enriched smectite clay preparations (series a).

Fig. 2: Decomposition of the LR medium by Mars soil in the Viking Labeled Release Experiment (VL-2), and in simulation experiments with sodium formate using iron oxides (maghemite, goethite, hematite and ferrihydrite) and iron carbonate (siderite) mixtures with iron saturated clay (series b and d respectively), and the iron oxides mixed with crude montmorillonite (SWy-1) (series c).
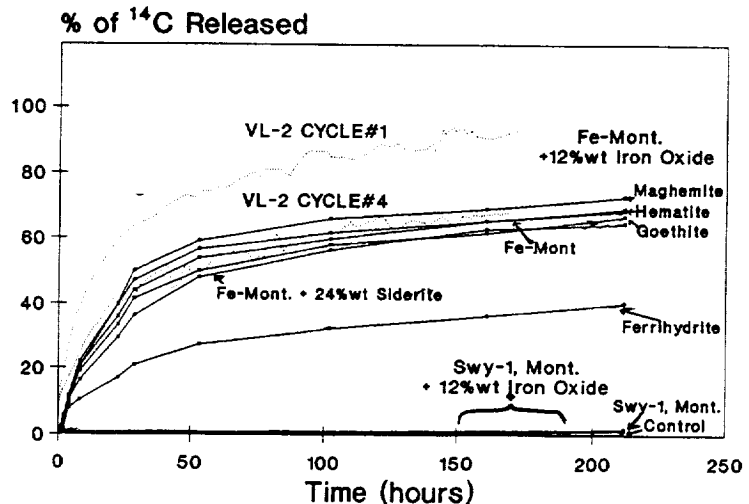
MARTIAN MANTLE PRIMARY MELTS

C.M. Bertka*, and J.R. Holloway Department of Geology, Arizona State University, Tempe, AZ 85287; *also at the Geophysical Laboratory, Carnegie Institution of Washington, 2801 Upton St. N.W., Washington D.C. 20008

INTRODUCTION:

Primary melts are liquid compositions in equilibrium with their mantle source region. Models that attempt to predict the diversity of lavas on a planet or outline the petrogenetic history of lavas require information about the chemical and physical properties of primary melts. These properties are determined by the bulk composition, modal assemblage, volatile content, and oxygen fugacity of the source region and by the degree of partial melting.

Most estimates of the bulk composition of the Martian mantle rely on calculations of mantle density. These calculations suggest that the Martian mantle is denser than the Earth's mantle, a difference that is attributed to an iron-enrichment of the Martian mantle(e.g.,1,2,3). Calculations of mantle density depend on knowledge of the mean moment of inertia of Mars. This value is poorly constrained and recently a lower estimate, which would result in a more Earth-like mantle iron abundance, has been proposed (4). However, if Mars is the parent body of SNC meteorites(5) then these samples help constrain the mantle composition independent of estimates of mantle density. Wanke and Dreibus (6) used element correlations between measured ratios in SNCs and chondritic abundances to predict a SNC parent body with a mantle enriched in iron relative to the earth. The purpose of this paper is to present our experimental melting phase equilibria data for an anhydrous Dreibus and Wanke mantle composition at 10, 20 and 30 kb.

EXPERIMENTAL TECHNIQUE:

Experiments were performed in an end-loaded piston cylinder apparatus with a 0.5" diameter solid-media pyrex-NaCl-AlSiMag cell assembly. Starting materials were synthesized from spec pure oxides ground under ethanol in an agate mortar for one hour , reduced in a gas mixing furnace (1000° C, fO_2 at one log unit below QFM) for 24 hours and reground in a carbide container to less than 5um. Approximately 10 mgs of the starting composition was sealed in graphite-lined platinum capsules. Run duration varied from 48 hours at near solidus temperatures to 1 hour at near liquidus temperatures.

RESULTS:

Phase equilibria data for the Dreibus and Wanke, (DW) mantle composition at 10, 20 and 30 kb are shown in Figure 1. Experimental Fe/Mg distribution coefficients for ol / opx and gt / cpx pairs in the subsolidus runs are in good agreement with previously determined values (7,8). A spinel lherzolite assemblage is stable to at least 20kb, but the subsolidus spinel phases are less than 10um in size and exhibit variations of up to 7 wt% in aluminum and chrome contents. Mass balance calculations to express the DW mantle composition as proportions of the analyzed subsolidus phases were performed with a least squares fit technique. In all cases the calculated modes duplicate the starting composition with a total error of less than 1.5 wt%, most of which can be attributed to poor spinel analysis.

Enough melt accumulated at the top of some of the charges run in the opx+ol+liq and the ol+liq fields that the resulting quench crystals + glass material could be analyzed by rastering a 2-um beam across a 20-um x 20-um area. The analyzed melts are komatiitic. Experimental Fe/Mg ol/melt and ol/opx distribution coefficients also compare favorably with previously determined values (9,7) and mass balance calculations duplicate the starting composition with a total error of less than 2.5wt%.

DISCUSSION:

Compared to the earlier model Martian mantle bulk compositions, (i.e. Morgan and Anders(2), Goettel(3)), and the proposed terrestrial undepleted mantle samples, (PHN 1611 (10), KLB-1(11)), the DW composition has a greater modal abundance of orthopyroxene (12) largely at the expense of olivine or clinopyroxene. Partial melting of a DW lherzolite assemblage produces a larger temperature interval of primary melts in equilibrium with only olivine and orthopyroxene. Our data indicates a minimum interval of 200° C at 10kb and 120° C at 20 kb. Experimental data for KLB-1 at 15kb (13) and PHN1611 at 20kb (14) indicate maximum olivine + orthopyroxene + melt intervals of 100°C. The primary melt compositions produced in this interval will be picritic to komatiitic. Tholeiitic and alkali basalt melts are expected to be produced at lower degrees of partial melting, before clinopyroxene or the aluminous phase are exhausted. However, the relative abundance of these primary magma types compared to the komatiitic

MARTIAN MANTLE PRIMARY MELTS
Bertka, C.M. and Holloway, J.R.

melts can not be evaluated without additional data. Although clinopyroxene is present in subsolidus experimental assemblages it is absent above the solidus except in two experimental charges from the spinel lherzolite field at 15 and 20kb. These charges were equilibrated at temperatures well above the solidus then lowered in temperature to the solidus. Their clinopyroxene compositions are very similar to those found in the subsolidus runs. This data suggest that clinopyroxene may melt out of the spinel lherzolite assemblage within 20° C of the solidus. Our previous experimental work (12) suggested that an iron-rich lherzolite assemblage would yield a picritic alkali basalt at small degrees of melting.

The surface features of Martian lava flows are often attributed to high eruption rates and/or low viscosity magmas (e.g.,16). Our previous work (17) suggested that the picritic alkali basalt produced at low degrees of partial melting at 23kb has a viscosity of 3 poise at source region pressure; similar in magnitude to its calculated 1atm. values at the same temperature. This viscosity is much smaller than that measured for a terrestrial tholeiite composition at 20kb and near liquidus temperatures, 25 poise(18) but similar in magnitude to 1atm. calculated values for a terrestrial alkali basalt at its 30kb liquidus temperature. Magma ascent rates or crystal fractionation processes in the two planets for any given primary melt type (i.e, alkali basalt, tholeiite,komatiite) may be more sensitive to gravitational differences between the two planets than to viscosity differences between the melts at their respective liquidus temperatures. Additional near solidus phase equilibria data for the model DW Mars mantle should reveal whether or not the bulk composition and resulting modal mineralogy favor the production of low viscosity picritic and komatiitic primary melts.

References. 1) McGetchin, T.R. and Smyth, J.R. (1978) Icarus 34, 512-536. 2) Morgan, J.W. and Anders, E. (1979) Geochim. Cosmochim. Acta 43, 1601-1610. 3) Goettel, K.A. (1981) Geophys. Res. Lett. 8, 497-500. 4) Bills, B.G. (1989) abst. Lunar and Planet. Sci. XX, 74. 5) McSween, H.R. (1985) Rev. Geophys. 23, 391-416. 6) Wanke, H. and Dreibus, G. (1988) Phil. Trans. R. Soc. Lond. A 325, 545-557. 7) Mori, T. and Green, D.H. (1978) J. Geol. 86, 83-97. 8) Ellis, D.J. and Green, D.H. (1979) Contrib. Mineral. Petrol. 71, 13-22. 9) Roeder, P.L. and Emslie, R.F. (1970) Contrib. Mineral. Petrol. 29, 275-289. 10) Nixon, P.H. and Boyd, F.R. (1973) in Lesotho Kimberlites, ed. P.H. Nixon. 11) Carter, J.L. (1970) Geol. Soc. Am. Bull. 81, 2021-2034. 12)Bertka, C.M. and Holloway, J.R. (1987) Proc. lunar Planet. Sci. Conf. 18, 723-739. 13) Takahashi, E. (1985) J. Geophys. Res. 91, 9367-9382. 14) Mysen, B.O. and Kushiro I. (1977) Amer. Mineral. 62, 843-865. 15) Schonfeld, E. (1979) abst. Lunar and Planet. Sci. IX, 1063. 16) Bertka, C.M, and Holloway , J.R. (1989) abst. Lunar and Planet. Sci. XX, 69. 17) Kushiro, I., Yoder, H.S. and Mysen, B.O. (1976) Jour. Geophys. Res. 81, 6351-6356. 18) Leshin, L.A., Holloway, J.R., and Bertka, C.M. (1988) abst. Lunar and Planet. Sci. XIX, 67.

Figure 1. DW Anhydrous Experimental Phase Assemblages
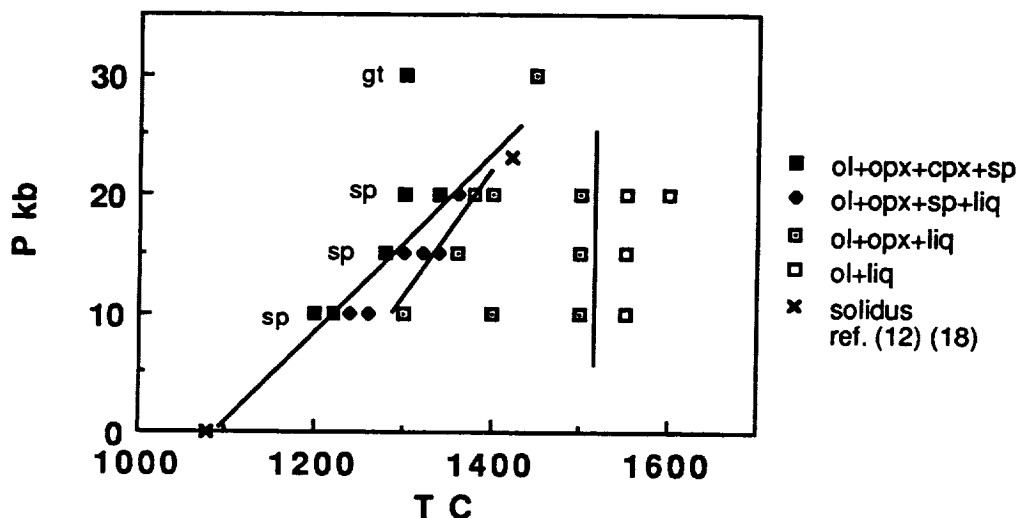
DIGITAL MOSAIC AND ELEVATION MODEL OF CENTRAL VALLES MARINERIS, MARS; L. M. Bertolini, A.S. McEwen, U.S. Geological Survey, Flagstaff, AZ 86001

We have geometrically controlled 143 Viking Orbiter 1 images to produce a digital mosaic of the central Valles Marineris region of Mars. The mosaic covers most of Ophir, Candor, and Melas Chasmata and covers approximately $+1^\circ$ to -15° latitude and 65° to 75° longitude. The image frames are PICNOS 910A01-917A20, red filter and nadir looking; illumination and phase angles both range from 55 to 65 degrees. Noise removal by box filtering [1], radiometric correction, and all other image processing were done by using the Planetary Image Cartography System (PICS). The image frames were transformed into sinusoidal Equal Area projections at a scale of 1/1024 degree/pixel (approximately 58 m/pixel) prior to mosaicking. The geometric control and format are consistent with those of the Mars Digital Image Model project [2,3].

We obtained measurements of landslides and other features from the controlled images using the photoclinometric program TVPROF (on single images) and the program TVSTEREO on pairs of images. For TVPROF [4], which produces topographic profiles, we used a variety of photometric models and parameters to constrain the slope values. TVSTEREO calculates relative heights. Measurements include those of landslide drops, deposit thicknesses, and slopes of canyon walls. The data will be used to refine estimates and to make additional ones of landslide volumes and yield strengths [5].

In addition, we prepared a digital elevation model of the region from -3° to -7.6° latitude and from 70° to 75° longitude from a 1:500,000-scale (200-m contour interval) topographic map [U.S.Geological Survey, work in progress]. The topographic map was first digitized into vector format, then transformed into raster format of the same map projection and scale as the digital mosaic; the contour lines were then interpolated to produce the digital elevation model. From the coregistered mosaic and digital topographic data, synthetic oblique views were generated from the north, south, east, and west. When producing an oblique view, we can specify viewpoint elevation and azimuth and vertical exaggeration. The oblique views provide versatile imaging of geologically important areas and their topography. These data will eventually be used to make 3-dimensional movies of the terrain.

REFERENCES

[1] Eliason, E. M., and McEwen, A.S. Adaptive box filters for removal of random noise from digital images. Photogrammetric Engineering and Remote Sensing (in press).

[2] Batson, R.M. (1987) Digital cartography of the planets: New methods, its status, and its future. Photogrammetric Engineering and Remote Sensing 53, 1211-1218.
[3] Edwards, K. (1987) Geometric processing of digital images of the planets. Photogrammetric Engineering and Remote Sensing 53, 1219-1222.
[4] Davis, P.A., and Soderblom, L.A. (1984) Modeling crater topography and albedo from monoscopic Viking Orbiter images. J. Geophys. Res. 89, B11, 9449-9457.
[5] McEwen, A.S. (1989) Mobility of large rock avalances: Evidence from Valles Marineris, Mars. Geology 17, 1111-1114.

PRELIMINARY QUANTITATIVE ASSESSMENT AND ANALYSES OF PHOBOS 88 TERMOSKAN OBSERVATIONS OF MARS; B. H. Betts, T. Svitek, M. L. Santee, B. C. Murray, D. Crisp, California Institute of Technology, D. A. Paige, University of California at Los Angeles, M. Naraeva and A. Selivanov, Institute of Space Devices, Moscow.

In February and March, 1989, the Termoskan instrument onboard the Phobos '88 spacecraft of the USSR acquired a limited set of very high resolution simultaneous observations of the reflected solar and thermal emission from Mars' equatorial region. We have analyzed quantitatively approximately 20% of the entire data set and here present three preliminary analyses: a comparison of Termoskan data with Viking Infrared Thermal Mapper (IRTM) data; an analysis of thermal infrared limb brightening seen on the morning limb and other preliminary limb analysis results; and an analysis of one observation of the shadow of the moon Phobos as observed on Mars by Termoskan.

THE EXPERIMENT: Termoskan was a two channel optical-mechanical scanning radiometer with one visible channel (0.5-1.0 μm and one thermal infrared channel (8.5-12.0 μm). The instrument was fixed to the spacecraft, pointing in the anti-solar direction. Resolution per pixel at nadir was 1.8 km for 3 of the 4 panoramas acquired and 300 meters for the remaining panorama.

COMPARISON WITH IRTM OBSERVATIONS: To determine the absolute accuracy of the Termoskan data set, we compared it with the well calibrated Viking IRTM measurements. We compared brightness temperatures from Termoskan infrared observations to brightness temperatures from IRTM's 11 micron channel (9.8 to 12.5 μm). We constrained the IRTM data to match approximately the Termoskan data in season (L_s), longitude, latitude, and local time of day. In order to compare the two data sets, we degraded the Termoskan resolution to a resolution comparable to Viking. Figure 1 shows a representative Termoskan-IRTM comparison which is consistent with other areas that we have compared. We find that the Termoskan brightness temperatures are approximately 3 K warmer than corresponding IRTM brightness temperatures; that relative features correlate very well in the two data sets; and that Termoskan sees thermal variations even at the limit of its spatial resolution.

TERMOSKAN LIMB PROFILES: Limb brightening in the Termoskan thermal infrared channel from the morning limb was consistently observed. Figure 2 shows a sample morning limb profile. We explain the peak in thermal brightness just off the limb as a consequence of an ice or dust haze in equilibrium with the atmosphere, which is warmer than the pre-dawn surface. Paige used a delta-Eddington spherical shell model developed for the Mars Observer limb sounder PMIRR (Pressure Modulator Infrared Radiometer), and found that a water ice haze with a scale height of 5 km (isothermal atmosphere at 200 K, surface at 175 K) could produce a thermal brightness signature matching the one in Figure 2. The visible channel defines a highly scattering atmosphere to extend 60 to 70 km above the limb. Figure 3 shows a sample evening limb profile. The absence of any infrared evening limb brightening is consistent with a surface which is warmer than the atmosphere . On the evening limb a high haze was observed which may correlate well with that seen by the Phobos '88 AUGUST experiment.

PHOBOS SHADOW MEASUREMENTS: Termoskan observed the shadow of Phobos on the surface of Mars during two of its four scans. Due to the scanning nature of the instrument and the similarity of the spacecraft's orbit to that of Phobos, the shadow appears elongated in the images. We have looked at one shadowed region south of Arsia Mons. We used the observed drop in visible flux within the shadowed area to model the solar insolation as a function of both actual time since the beginning of eclipse and position in the scan. We then used this in an adaptation of the Clifford et al., 1987 one dimensional, finite difference thermal model for a homogeneous surface [1]. By comparing the model results with the temperature drops observed in the infrared scan we find thermal inertias varying from 0.7 to 1.1 (10^{-3} cal cm^{-2} s$^{-1/2}$ K^{-1}). These values of thermal inertia are lower by factors of 2 to 4 compared to thermal inertias derived from Viking IRTM measurements [2] for the same area. Viking-derived inertias are sensitive to the upper few centimeters of the surface, whereas the Phobos shadow measurements are sensitive only to the upper tenths of a mm of the surface due to the short duration of the

eclipse. Our results imply that there is a thin layer of highly insulating material, for example a thin, loosely packed dust layer, on the surface which overlies a layer of less insulating material.

REFERENCES: (1) Clifford, S.M., C.J. Bartels, and E.P. Rübenstein (1987), Lunar and Planetary Institute; (2) Kieffer, H.H., T.Z. Martin, A.P. Peterfreund, B.M. Jakosky, E.D. Miner, F.D. Palluconi (1977), Journal of Geophysical Research, 82 (28), pp. 4249-4291.

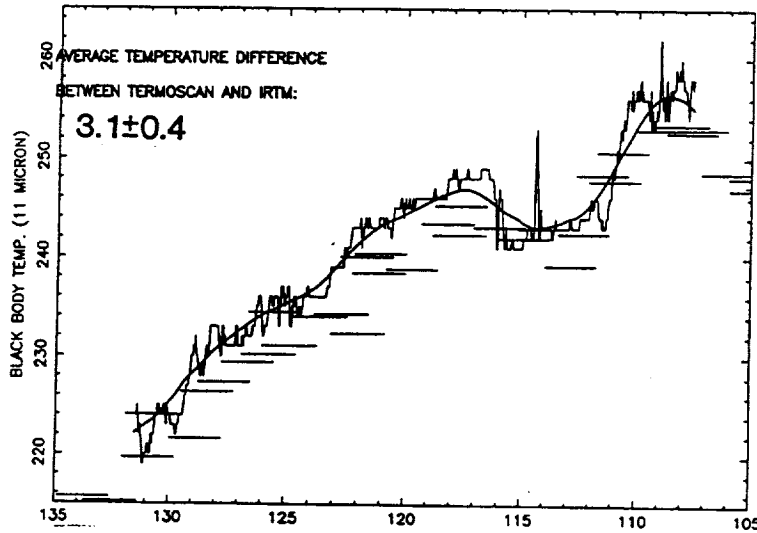d': −18°0±1°0 LAT.; TERMO. DATA: 67 PIXELS SQUARE AVG.; ±30 MIN.

Figure 1: Comparison of Termoskan data with analogous IRTM data for a 2 degree wide strip of constant latitude centered on -18 degrees. The dark line represents a sliding boxcar average of Termoskan data which has been averaged in 2 x 2 degree squares. The lighter line is a 1 pixel Termoskan strip for reference. The points represent IRTM data with the error bars representing the footprint of each IRTM data point. IRTM data is constrained to match the Termoskan data to within ±10 degrees of L, and to within ±30 minutes of local time. After comparing each IRTM point with the averaged Termoskan point of the same longitude, the average temperature difference between Termoskan and IRTM is 3.1±0.4 K with the Termoskan temperatures being warmer. Local time of day in the data shown ranges from about 8.5 to 10.3.
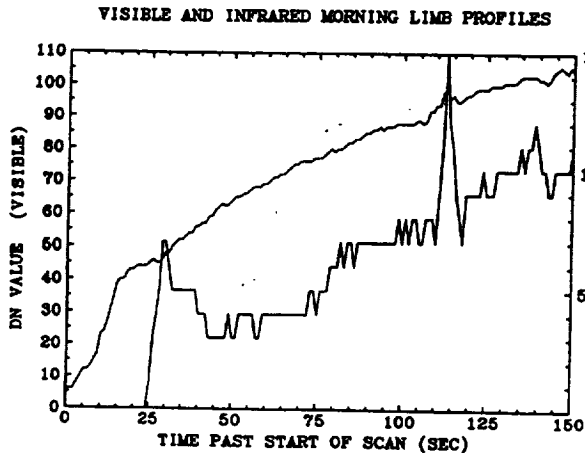
VISIBLE AND INFRARED MORNING LIMB PROFILES

Figure 2: A single morning limb profile for both the visible (dashed curve) and the infrared (solid curve) channels. The solid limb was encountered at approximately 26 seconds after the start of the scan.

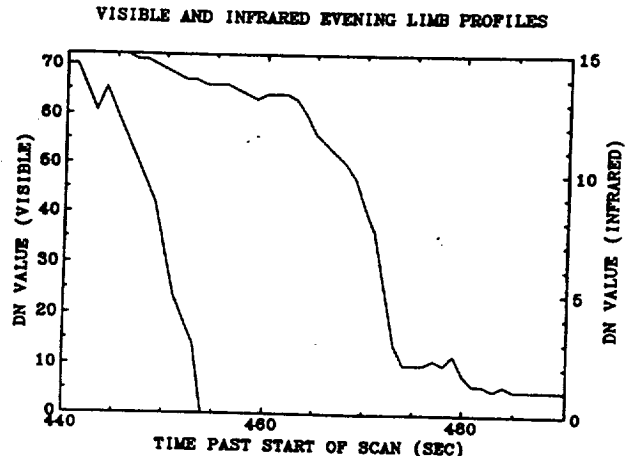VISIBLE AND INFRARED EVENING LIMB PROFILES

Figure 3: A single evening limb profile for both the visible (dashed curve) and the infrared (solid curve) channels. Note that the times on the horizontal axis are local to the particular data file and do not represent actual times along the scan. Note the peak in visible brightness at 479 seconds which is a distinct cloud feature.